



## Green Chemistry

### ARTICLE

# Synthesis of Perfectly Ordered Mesoporous Carbons by Water-assisted Mechanochemical Self-assembly of Tannin

Jimena Castro-Gutiérrez,<sup>a</sup> Angela Sanchez-Sanchez,<sup>a</sup> Jaafar Ghanbaja,<sup>a</sup> Noel Díez,<sup>b</sup> Marta Sevilla,<sup>b</sup> Alain Celzard<sup>a</sup> and Vanessa Fierro<sup>a\*</sup>

Received 00th January 20xx,  
Accepted 00th January 20xx

DOI: 10.1039/x0xx00000x

www.rsc.org/

A simple, green, one-pot mechanochemical synthesis method for preparing perfectly ordered mesoporous carbons (OMCs) by ball-milling is presented herein. Mimosa tannin (T) and Pluronic® F127 (P) are used as carbon precursor and as mesopore-directing agent, respectively. Water (W) is used to promote micelles formation but also the interaction between T and P; no crosslinker is used and drying or curing steps before carbonization are not needed either. The experimental conditions, such as the milling time, the pH of added W and the P:W ratio are optimized to obtain perfect 2D hexagonal OMCs with BET areas as high as 588 m<sup>2</sup> g<sup>-1</sup> after carbonization at 900 °C. Carbonization temperatures up to 1500 °C or activation allow increasing further the surface area, up to ~1900 m<sup>2</sup> g<sup>-1</sup>, while maintaining the ordered mesoporous structure. These materials should find relevant applications in environmental remediation strategies for oil spills, in selective CO<sub>2</sub> adsorption from humid gases or as electrodes of supercapacitors.

## Introduction

The synthesis of ordered mesoporous carbons (OMCs) is a topic of great importance due to their potential application in biosensors,<sup>1</sup> adsorbents for enzymes,<sup>2</sup> oil spills removal,<sup>3,4</sup> CO<sub>2</sub> adsorption,<sup>5–7</sup> or as electrodes for supercapacitors,<sup>8,9</sup> batteries<sup>9</sup> and fuel cells.<sup>10,11</sup> OMCs are usually produced by either hard or soft templating. In the former method, silica particles,<sup>12</sup> zeolites<sup>10,12</sup> or biosourced materials<sup>13–15</sup> are coated with a carbon precursor and submitted to carbonization followed by template removal using HF or NaOH; the resultant OMC is a negative replica of the template. In the latter method, an amphiphilic surfactant, usually a triblock copolymer, is used in solution to form micelles that act as templates for the carbon precursor; a subsequent pyrolysis process then eliminates the surfactant, producing mesoporosity in the resultant carbon materials.<sup>2</sup> Whether through hard or soft templating, OMC synthesis generally uses molecules of petrochemical origin (like resorcinol or phenol) as carbon precursor, takes several days and involves the use of hazardous substances such as formaldehyde, commonly used as a crosslinker, or HF or NaOH, used for leaching out the hard templates.

Pluronic® F127 (P) is often used in soft-templating methods, and different precursors and/or precursor to surfactant ratios can result in different orderings; among the latter, the 2D

hexagonal array is one of the most commonly found. For example, by using phenol-formaldehyde resins with P, it is possible to obtain OMCs with cubic or hexagonal structure by changing the precursor to surfactant ratio.<sup>16,17</sup> Moreover, OMCs with 2D hexagonal symmetry prepared by evaporation-induced self-assembly (EISA) were obtained using a resorcinol-formaldehyde resin and P.<sup>18</sup> Tannin as carbon precursor was used with P and without any crosslinker in an EISA process to obtain OMCs with a hexagonal structure.<sup>19</sup> OMCs having a hexagonal array were also produced by self-assembly of P and mimosa tannin in an aqueous medium.<sup>20</sup>

Solid-state synthesis methods are attracting increasing interest because: (i) they are either liquid-assisted (with low amounts of solvents) or even solvent-free<sup>21–24</sup> (ii) the synthesis time is shorter compared to methods based on chemistry in solution,<sup>21,22</sup> (iii) they are cheaper and more environment-friendly as they comprise fewer synthesis steps.<sup>24,25</sup> In particular, mechanochemical synthesis, by which mechanical energy is absorbed for synthesizing the material, has been used to produce ceramics,<sup>23</sup> metal alloys,<sup>26</sup> organic materials<sup>22</sup> and more recently OMCs.<sup>25,27,28</sup> Mechanical energy can be provided by shearing, stretching or grinding.<sup>21</sup> It has been reported that solvent-free hand-grinding of P in the presence of resorcinol and terephthalaldehyde produce OMCs having either cubic or hexagonal structures by changing the initial amount of P; replacing terephthalaldehyde by formaldehyde in liquid-assisted synthesis produced a material with hexagonal structure.<sup>25</sup> Ball-milling of P, resorcinol, terephthalaldehyde, and melamine was also used to synthesize nitrogen-doped OMCs with a hexagonal structure.<sup>27</sup> In these studies, a curing or aging step of the material at low temperature (80 or 100 °C) was needed before carbonization. Furthermore, OMCs were

<sup>a</sup> *Institute Jean Lamour, UMR CNRS, University of Lorraine, ENSTIB, 27 Rue Philippe Séguin, BP 21042, 88051 Epinal Cedex 9, France.*

<sup>b</sup> *Instituto Nacional del Carbón (CSIC), P.O. Box 73, Oviedo, 33080, Spain.*

Electronic Supplementary Information (ESI) available: Supplementary figures and tables and demonstrative videos. See DOI: 10.1039/x0xx00000x

obtained by ball-milling tannin, P and metal acetates used as crosslinkers; in this case, washing and drying steps before carbonization were again required.<sup>28</sup> Nevertheless, ball-milling thus appears as a suitable method for synthesizing OMCs because it can provide higher energy and repeatability than hand-grinding,<sup>22</sup> and it has a great industrial potential as it reduces the energy requirements related to solvent production, purification, and recycling.<sup>21</sup>

In the present study, we report on a green one-pot method, schematized on Figure 1a, for preparing OMCs with a 2D hexagonal structure using a planetary ball mill. Mimosa tannin, a non-toxic and renewable material, was used as carbon precursor together with Pluronic® F127 (P) as pore-directing agent. No crosslinker was required, but only a small amount of water (W) was added and no curing or drying steps were needed either. The impact of key process parameters such as milling time, pH, P:W weight ratio and carbonization temperature on the porous structure of the resultant carbons was carefully analysed, aiming to produce the most ordered mesoporous carbon.

## Results and discussion

To study the effect of milling time, mechano-synthesis of the materials was carried out by ball-milling the same quantities (2 g) of tannin (T), Pluronic® F127 (P) and water (W) during times ranging from 30 to 120 min. The resultant paste-like materials were then submitted to carbonization at 900 °C. Samples were labelled T2P2W2\_t, where “t” accounts for the milling time in minutes, and the final carbon materials were identified by adding a “C” to the sample names. Figure 1b,c shows the changes of N<sub>2</sub> adsorption-desorption isotherms and derived pore-size distributions (PSDs) in the mesoporous range as a function of milling time and Table S1 in the Electronic Supplementary Information (ESI) shows the corresponding pore texture parameters obtained from N<sub>2</sub> and CO<sub>2</sub> adsorption-desorption isotherms. The  $A_{BET}$  ranged from 484 to 553 m<sup>2</sup> g<sup>-1</sup>, and no clear trend could be observed. However, 60 min appeared as an optimum milling time for obtaining the highest

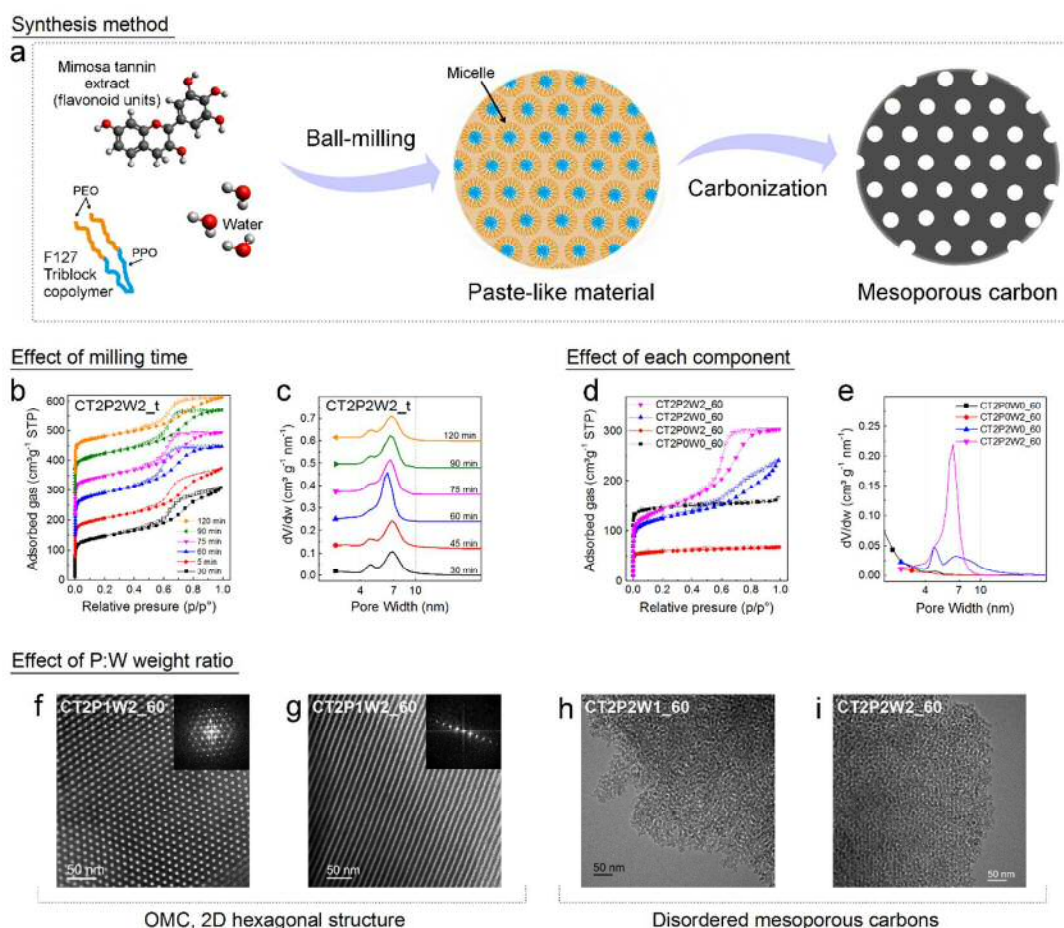


Figure 1. (a) Schematic of the mechano-synthesis method. N<sub>2</sub> adsorption-desorption isotherms and corresponding PSDs for: (b,c) CT2P2W2\_t samples synthesized at different milling times (t ranges from 30 to 120 min), for easier viewing the curves were shifted with respect to each other by 70 cm<sup>3</sup> g<sup>-1</sup> STP for isotherms and by 0.12 cm<sup>3</sup> g<sup>-1</sup> nm<sup>-1</sup> for PSDs; (d,e) CT2P2W2\_60 and of carbonized reference samples CT2P0W0\_60, CT2P0W2\_60, and CT2P2W0\_60. TEM-Bright field micrographs of: (f) transversal and (g) longitudinal views of CT2P1W2\_60; (h) CT2P2W1\_60; and (i) CT2P2W2\_60. The insets in (f,g) represent the corresponding FFT of CT2P1W2\_60.

mesopore fraction (Table S1). In addition, materials milled during 30 or 45 min presented PSDs with two distinct peaks: increasing the milling time up to 60 min decreased the first peak to just a shoulder, but a longer milling resulted in broader PSDs and in the reappearance of the first peak (Figure 1c). Therefore, it can be assumed that, up to 60 min, the milling process decreased the particle size of T and P powders and thus improved their intimate mixing. As a consequence, contact area and interaction between the components increased,<sup>21</sup> thereby favouring the creation of hydrogen bonds between T and P, as confirmed below by FTIR spectra. Longer milling times may produce the destabilization of micelles and hence explain the two peaks of the PSD.

To reveal the effect of each component of the mixture on the structure of the final carbons, the milling time was fixed at 60 min, and three reference samples were prepared by removing P, W, or both (T2P0W2\_60, T2P2W0\_60, and T2P0W0\_60, respectively). After carbonizing them at 900 °C, those samples were thus compared to CT2P2W2\_60. Figure 1d,e shows their adsorption-desorption isotherms and the corresponding PSDs. CT2P0W0\_60 and CT2P0W2\_60 presented type I isotherms that are typical of purely microporous solids. They show that, in the absence of P, adding W decreased the  $A_{BET}$  of the final carbon material from 578 to 231 m<sup>2</sup> g<sup>-1</sup>, thus evidencing that carbonizing a dry powder instead of a paste-like agglomerated material produced a higher microporosity. This effect might be due to the easier release of volatiles from a powder. CT2P2W0\_60 and CT2P2W2\_60 presented type IV isotherms, typical of mesoporous materials. They show that, whether W was present or not, adding P was necessary for producing mesopores; however, the material prepared without water, CT2P2W0\_60, had a broader PSD and a much lower  $V_{meso}$  than CT2P2W2\_60 (see again Table S1). Hence, it can be concluded that both P and W are simultaneously needed for achieving mesoporous materials with the narrowest mesopore-size distribution. No mesopores were indeed formed without P, whereas W was required to form micelles and to allow the best interaction between T and P.

Fourier-Transform IR (FTIR) spectra of reference samples and samples prepared at various milling times, before carbonization, are shown in Figure S1 and Figure S2 (in the SI), respectively. The FTIR spectrum of a sample prepared by milling only 2 g of P and 2 g of W for 60 min (T0P2W2\_60), i.e., without T, is also shown, and the assignment of peaks is provided in Table S2.<sup>29–31</sup> Samples containing P presented a broader band around 3300 – 3400 cm<sup>-1</sup>; this finding was expected as it is related to polymeric OH stretching.<sup>31</sup> For the samples obtained at different milling times (Figure S2), an increase of intensity of polymeric stretching peak was observed. Since the ratio of components during the mechanosynthesis was kept constant, this finding suggests the formation of hydrogen bonds.<sup>28,32</sup>

Thermogravimetric analysis (TGA) performed to study the thermal stability of samples led to the results shown in Figure S3, where samples are compared after subtraction of the mass loss attributed to the evaporation of water and further

normalization. The same behaviour of mass loss is observed for T2P0W0\_60 and T2P0W2\_60 samples (Figure S3a), revealing that the differences of the observed carbon yield, 41 and 26%, respectively, are only related to the initial amount of water in them. Figure S3a also shows that a peak of mass loss at ~260 °C for T2P0W0\_60 vanished when adding P to the formulation, implying that the interaction of P with T improves the thermal stability at this temperature. For T2P2W0\_60 and T2P2W2\_60, i.e., for samples containing P, an intense peak of differential mass loss was observed when the temperature reached 400 °C, due to the degradation of Pluronic,<sup>20</sup> after which the material remained fairly stable until 900 °C. Even more, T2P2W0\_60 and T2P2W2\_60 have identical mass loss curves when compared on dry basis, confirming that the major role of W during the synthesis is to form micelles and to improve the interaction between T and P, affecting in this way the resultant mesopore structure but not the thermal stability of the material. Changing the milling time did not seem to have any significant effect on the thermal stability of the materials since similar curves of mass loss were obtained for all samples with milling times ranging from 30 to 90 min (Figure S3b). This finding is in agreement with the carbonization yields that remained constant for all tested milling times. Therefore, it can be stated again that the milling time only modifies the resultant mesopore structure.

Formerly published studies showed that a low pH favours the self-assembly of surfactants with carbon precursors,<sup>33</sup> thereby affecting the textural properties of the final carbon materials.<sup>34</sup> The effect of pH was investigated herein by, instead of adding 2 g of W, adding 2 g of aqueous HCl solutions with pH values ranging from 0 to 4. All samples were then milled for 60 min, carbonized at 900 °C, and labelled CT2P2pHx\_60, where “x” stands for the pH of the added solution; Figure S4 shows their N<sub>2</sub> adsorption-desorption isotherms and corresponding PSDs. The sample prepared at pH 0 presented a rather different mesopore-size distribution, with two overlapping peaks, the highest centred at 4.7 nm and a lower one centred at 5.4 nm. The highly acidic medium present during the synthesis of CT2P2pH0\_60 may have produced significant T autocondensation, a well-known behaviour of tannin at low pH, thus preventing it from having a good interaction with P, hence its different PSD. Overall, when compared to CT2P2W2\_60, i.e., with the sample at unaltered pH, no significant change of porous texture was observed (Table S1). In addition, the modification of the pH of added water during synthesis did not improve the ordering of the resultant carbon materials. In particular, CT2P2pH1\_60 resembles the most to CT2P2W2\_60 sample from the point of view of PSD and TEM images (Figure S4 and S5). Thus, for simplicity, the following studies described below were carried out using only pure distilled water.

Since changes of surfactant concentration in aqueous solutions can give rise to micellar, cubic, rod-like or hexagonal phases,<sup>35–46</sup> the effect of the P:W weight ratio on the resultant carbon materials was investigated at constant milling time of 60 min. The corresponding samples were named CT2PnWm\_60,

according to their n:m (P:W) weight ratio, expressed in g/g. First, the amount of P was changed from 1 to 3 g while keeping W constant and equal to 2 g, Figure S6a,b shows the nitrogen adsorption-desorption isotherms and the PSDs. Low amounts of P (0.5 g) did not allow the formation of mesopores since CT2P0.5W2\_60 adsorption-desorption isotherm is a type I, typical of microporous materials. P amounts from 1 to 2 g produced type IV isotherms with H2 loops, while higher amounts (up to 3 g) produced H4 loops with broader and bimodal PSDs. Therefore, a minimum of P was necessary to form micelles but an optimum was found to exist for getting unimodal, well-defined PSDs. As was concluded with P, when changing the amount of W from 1 to 3 g while maintaining P constant and equal to 2 g, there seems to be an optimum of 2 g of W for getting type IV isotherms and narrow PSDs. Figure S6c,d shows the nitrogen adsorption-desorption isotherms and PSDs obtained. Moreover, Figure 1f-i shows TEM images of CT2P1W2\_60, CT2P2W1\_60, and CT2P2W2\_60. Transversal and longitudinal sections of CT2P1W2\_60, together with the corresponding Fast Fourier Transforms (FFT) (Figure 1f,g and respective insets), revealed that the sample possesses a

perfect 2D hexagonal mesoporous structure. On the contrary, CT2P2W1\_60 and CT2P2W2\_60 (Figure 1h,i) have bimodal PSDs and show a disordered mesostructure at long range.

In order to improve our understanding of these phenomena and to optimize the synthesis method, a second set of 16 new carbon materials was synthesized. The PSDs curves of all 28 materials were deconvoluted and the maximum height (M), the full width at half-maximum (FWHM) and the peak position (PP) of the PSDs peaks were calculated. Examples of those deconvolutions are presented in Figure S7 and Table S3 reports the peak parameters thus obtained. Figure 2a shows a contour graph of the M / FWHM ratio, only considering the highest peak in the case of bimodal PSDs. This ratio indeed characterizes the shape of the PSD peaks, and the higher is its value, the higher and the narrower is the peak. The experimental P:W ratios tested are also represented using different symbols for separating purely microporous materials, i.e., without peaks of PSD in the mesoporous range (M = 0), from those having unimodal or bimodal mesopore size distributions. A ring-like plot was observed, indicating that unimodal PSDs are found in limited ranges of values of P

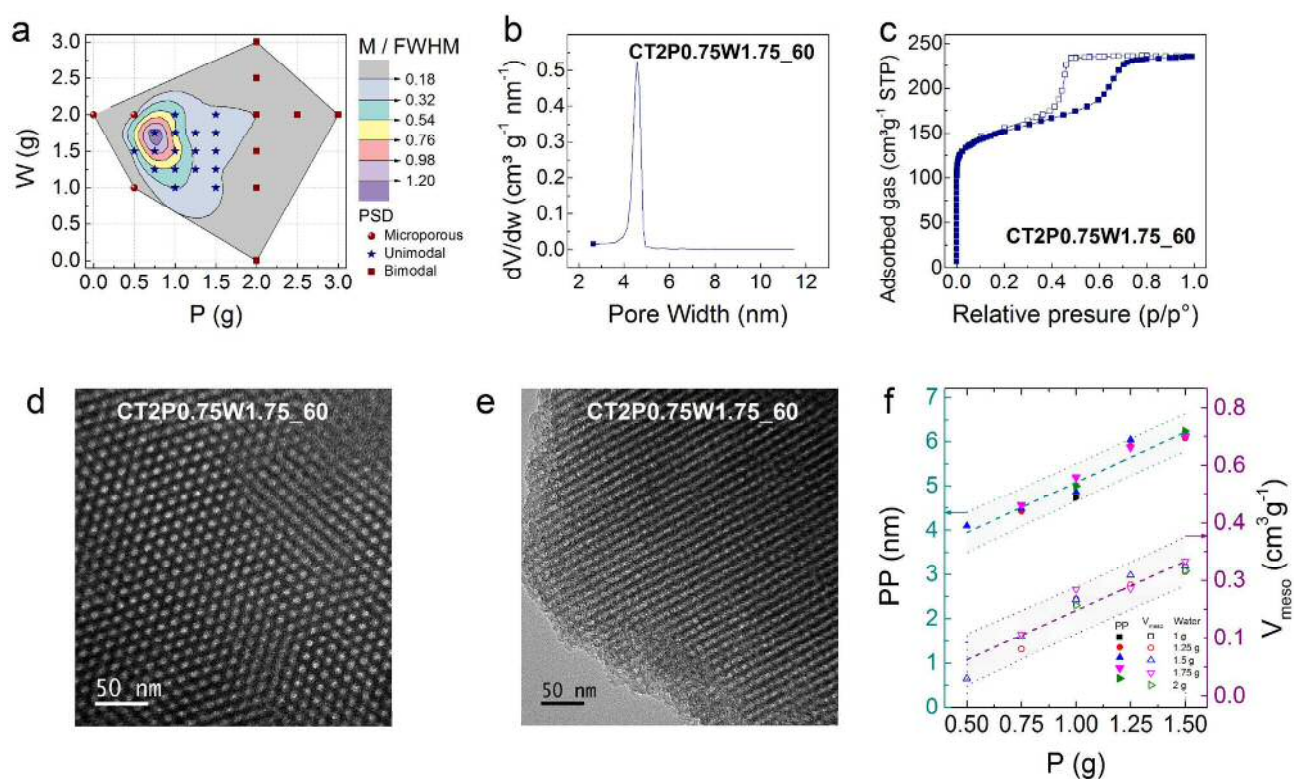


Figure 2. (a) Contour plot of the ratio M / FWHM of peaks obtained by deconvolution of the PSDs of samples synthesized using different P:W weight ratios and 60 min of ball-milling. The experimental P:W ratios tested are represented by points for purely microporous materials (M=0), and by stars and squares for unimodal and bimodal mesoporous distributions, respectively. (b) Highest and narrowest PSD of this study and (c) corresponding N<sub>2</sub> adsorption-desorption isotherms, found for sample CT2P0.75W1.75\_60 (located in the central region of the ring-like contour graph in (a)). (d,e) TEM-bright field micrographs confirming the 2D hexagonal structure of the same sample. (f) Peak position (PP, solid symbols) and mesopore volume ( $V_{meso}$ , hollow symbols) as a function of the initial mass of P and W; linear fits and corresponding 95 % prediction intervals (dashed and dotted lines, respectively) are presented for both quantities.

and W. Therefore, a single mesopore size, corresponding to PSDs with a unique and intense peak, can be obtained in the

range of P and W amounts located in the small area outlined by the central rings. The PSD having the highest intensity and

the narrowest peak was found for the sample CT2P0.75W1.75\_60 (Figure 2b). The corresponding  $N_2$  adsorption-desorption isotherms are shown in Figure 2c, and TEM images confirmed the 2D hexagonal, perfectly ordered structure of the material (Figure 2d,e).

In addition, the PP of unimodal PSDs was found to increase linearly with the amount of surfactant, and the  $V_{meso}$  followed a similar trend. Figure 2f shows that the PP varied from 4.1 to 6.2 nm while the  $V_{meso}$  varied from 0.12 to 0.35  $cm^3 g^{-1}$ . A similar behavior has been reported for 2D hexagonal mesoporous carbons self-assembled by P and using resorcinol-furfural or resorcinol-formaldehyde as carbon precursor, where a slight increase of pore volume and pore size with the P:carbon precursor ratio was observed.<sup>47–49</sup> These phenomena can be related to the degree of swelling of the PEO chains in the triblock copolymer. Higher amounts of P reduces the amount of water available to swell the PEO chains, increasing

the aggregation number and lowering the curvature of the hydrophilic/hydrophobic interface, and as a result the micelle size increases.<sup>47,50,51</sup> The  $V_{\mu,NLDFT}$  were mainly unaffected by the changes of P:W ratio and  $A_{BET}$  remained around 500  $m^2 g^{-1}$  for all samples (see Table S4). It thus appears that, through the variation of the P:W ratio, it is possible to tune the parameters of the ordered mesoporous structure, such as mesopore volume and size, without an impact on the microporosity.

T2P1W2\_60 was subjected to higher carbonization temperatures, up to 1500 °C, to test the thermal stability of the mesostructure and to study some possible changes in pore texture. When heated up from 900 to 1500 °C, type IV isotherms were obtained in all cases as shown in Figure S8 along with their corresponding PSDs, and a 2D hexagonal structure was further corroborated by TEM images (Figure 3a). A slight widening of the mesopores with temperature, from 5

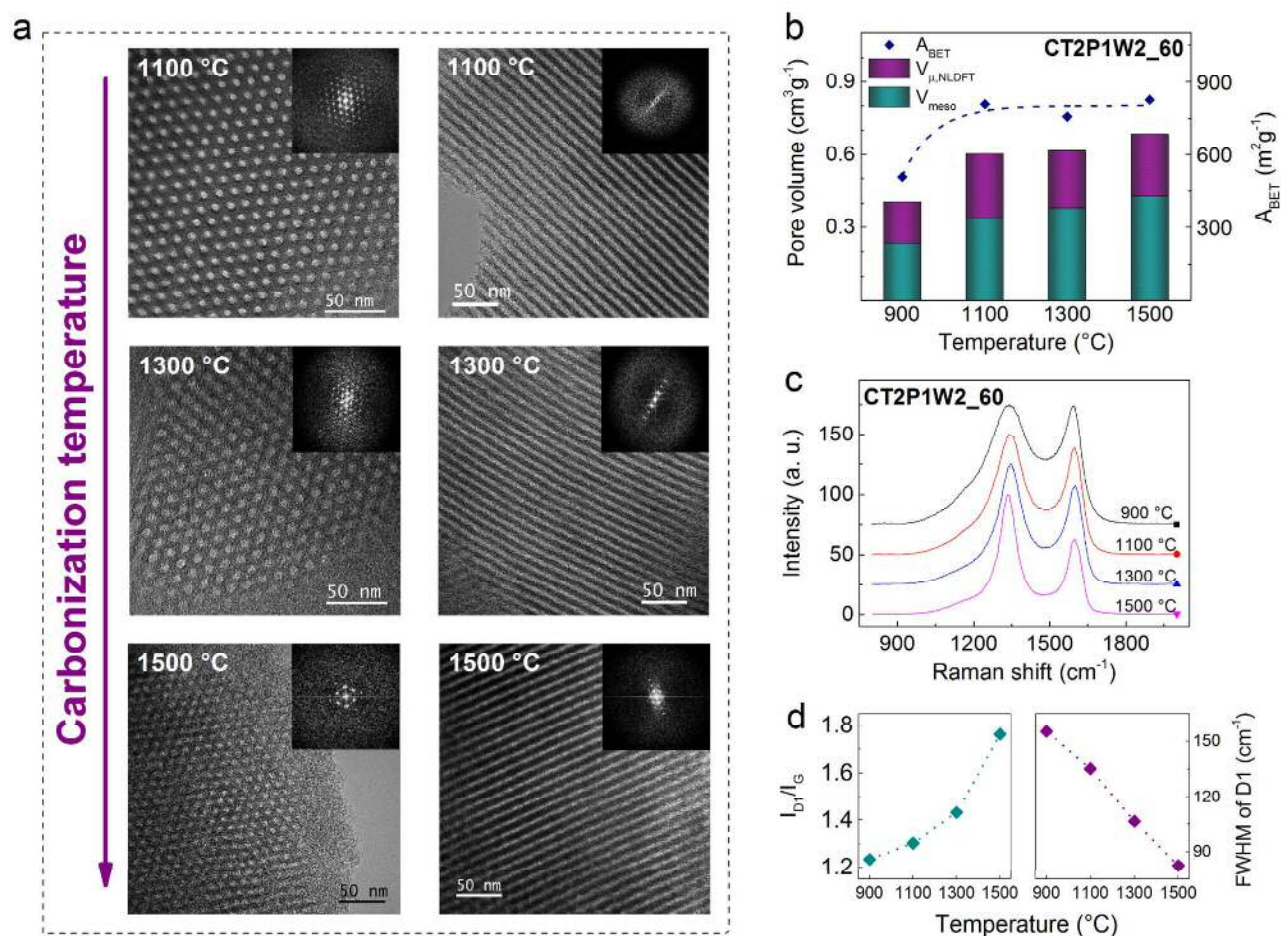


Figure 3(a) TEM-bright field micrographs of CT2P1W2\_60 pyrolyzed at 1100, 1300 and 1500 °C; the corresponding FFT are shown in the insets. (b) BET area and micro and mesopore volume of CT2P1W2\_60 as a function of pyrolysis temperature; the dotted line provides only a guide for the eye. (c) Raman spectra of CT2P1W2\_60 pyrolyzed at different temperatures, presented with a shift of 20 a. u. of intensity with respect to each other, for easier viewing; (d) D<sub>1</sub>/G intensity ratio and full width at half-maximum (FWHM) of the D<sub>1</sub> band as a function of temperature.

to 5.4 nm, can be observed from the PSDs (Figure S8b). Besides, Figure 3b shows the evolution with temperature of  $V_{\mu,NLDFT}$  and  $V_{meso}$  as well as the changes of  $A_{BET}$ . An increase

of  $V_{meso}$  with temperature was observed, from 0.24 to 0.43  $cm^3 g^{-1}$ . From 900 to 1100 °C, a development of microporosity occurred, reflected by an increase of  $V_{\mu,NLDFT}$  from 0.17 to

0.26 cm<sup>3</sup> g<sup>-1</sup> and thus by an increase of  $A_{BET}$ . However, higher temperatures had no significant impact on these quantities, in the range from 1100 to 1500 °C their values remained at  $0.25 \pm 0.02$  cm<sup>3</sup> g<sup>-1</sup> for  $V_{\mu,NLDFT}$  and at  $797 \pm 41$  m<sup>2</sup> g<sup>-1</sup> for  $A_{BET}$ . Aside from the pore texture characteristics, Raman spectra of CT2P1W2\_60 samples treated at different temperatures and given in Figure 3c, show that these OMCs are poorly crystallized at the nanoscale. All samples indeed displayed the typical spectra of highly disordered carbon, where the D<sub>1</sub> band is more intense than the G band<sup>20,52–55</sup> (see Figure S9 for detailed deconvolution of spectra). Due to the phenolic nature of tannin, all materials were non-graphitisable and were in the carbonization regime within the present experimental conditions, for which the intensity of the D<sub>1</sub> band (~1345 cm<sup>-1</sup>) increases with temperature. Thus, the increase of the D<sub>1</sub>/G intensity ratio ( $I_{D1}/I_G$  in Figure 3d), associated with an obvious narrowing of the D<sub>1</sub> band (FWHM of D1 in Figure 3d) at higher temperatures, indicates an increase of the crystallite size and hence an improvement of the long-range order in the carbon.<sup>55</sup>

To further study the physicochemical characteristics of these materials and suggest possible applications for specialist working in other fields, measurements of the water contact angle (WCA) were carried out. Figure 4a shows that the WCA on CT2P1W2\_60 was as high as 157° and it only slightly decreased to 147° when pyrolysis temperature was increased up to 1500 °C. A video provided as SI shows the low affinity of the water drop by the surface, the drop remained attached to the needle when it was pulled up from the surface and the volume of the drop had to be double up to 4 μL to get it on the surface and measure the WCA. These very high WCAs are in the range of materials used for efficient oil/water separation based on graphene oxide aerogels<sup>3</sup> or polymers.<sup>4</sup> Therefore, a simple proof of concept for organics removal in water phase was performed. For this purpose, 0.3 mL of heptane were poured in 1.5 mL of water, afterwards a piece of 100 mg of agglomerated CT2P1W2\_60 was introduced. Total heptane removal was obtained in less than 50 s, as showed in Figure 4b and in the video provided as SI. The ability to selectively remove oil/organic solvents while repelling water is an interesting feature of these materials that merits further research due to the fact that the use of sorbent materials is considered one of the most efficient and cost-effective methods among the environmental remediation strategies for oil spills.<sup>56,57</sup>

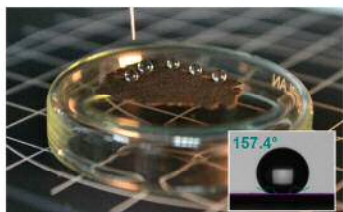
All the OMCs synthesized herein presented a high  $V_{meso}$  sometimes associated with an ordered mesostructure; both

factors should facilitate gas diffusion to the ultra-microporosity. In a previous study, phenolic resin-based mesoporous carbons were tested as CO<sub>2</sub> adsorbents after activation, CO<sub>2</sub> uptakes (at 0.1 MPa and 0 °C) were comparable to the values achieved for MOFs.<sup>5</sup> In contrast to MOFs, our OMCs are much cheaper and insensitive to humidity. Figure 4c shows the CO<sub>2</sub> adsorption of the OMCs developed herein after either physical activation with CO<sub>2</sub> or chemical activation with KOH and potassium acetate. CO<sub>2</sub> storage increased from 2.8 to 5.6 mmol g<sup>-1</sup> as a function of  $V_{\mu,NLDFT}$ , these CO<sub>2</sub> capacities were in the range of the values reported in the open literature.<sup>5–7</sup>

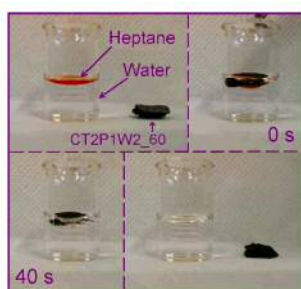
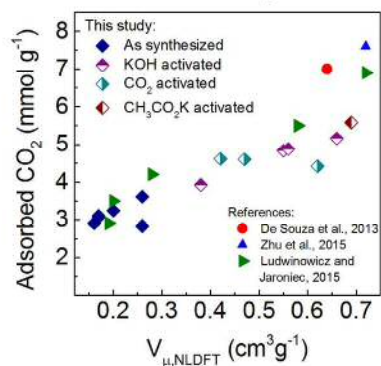
To explore the applications of the tannin-derived OMCs as electrodes for supercapacitors, sample CT2P0.75W1.75\_60 was subjected to CO<sub>2</sub> activation at 900 °C for 75 min, and the resultant activated OMC was labelled A75\_CT2P0.75W1.75\_60. This was done due to the rather modest  $A_{BET}$  of as synthesized materials and considering that it is well known that the capacitance of electrochemical double layer capacitors is related to the surface area of the electrode material. As calculated from N<sub>2</sub> isotherms and their corresponding PSDs in Figure S10,  $A_{BET}$  increased considerably, from 567 to 1867 m<sup>2</sup> g<sup>-1</sup>, and its  $V_{\mu,NLDFT}$  increased from 0.20 to 0.62 cm<sup>3</sup> g<sup>-1</sup>. An increase of  $V_{meso}$  from 0.16 to 0.55 cm<sup>3</sup> g<sup>-1</sup> resulted from a widening of the PSD, but without changing the peak position that remained at 4.6 nm. The electrochemical characterization was carried out on A75\_CT2P0.75W1.75\_60 in aqueous and organic electrolytes; specific cell and electrode capacitances,  $C_{cell}$  and  $C_e$ , respectively, and energy and power densities were calculated. It is worth noting that the electrodes made from A75\_CT2P0.75W1.75\_60 showed an improved hydrophilicity as they were wetted quickly when put in contact with the aqueous electrolyte.

Figure 4d shows the corresponding CVs at increasing sweep rate using aqueous electrolyte (1 M H<sub>2</sub>SO<sub>4</sub>),  $C_{cell}$  ranged from 41 to 27 F g<sup>-1</sup> ( $C_e$  from 163 to 108 F g<sup>-1</sup>) and the square-shape voltammograms obtained up to 1 V s<sup>-1</sup> indicated fast charge propagation. Also in aqueous electrolyte, Figure 4e shows the GCD curves at different current densities where the good capacitive behaviour is confirmed by the symmetrical charge/discharge voltage profiles, with a small IR drop regardless of the current density. Figure S11a shows the evolution of  $C_{cell}$  as a function of current density calculated from GCD tests at current densities ranging from 0.2 to 170 A g<sup>-1</sup>. As expected, the improved hydrophilicity together with the high surface area of the activated OMC resulted in high values

## a Hydrophobicity



## b Adsorption of heptane

c Adsorption of CO<sub>2</sub>

## Electrodes for supercapacitors

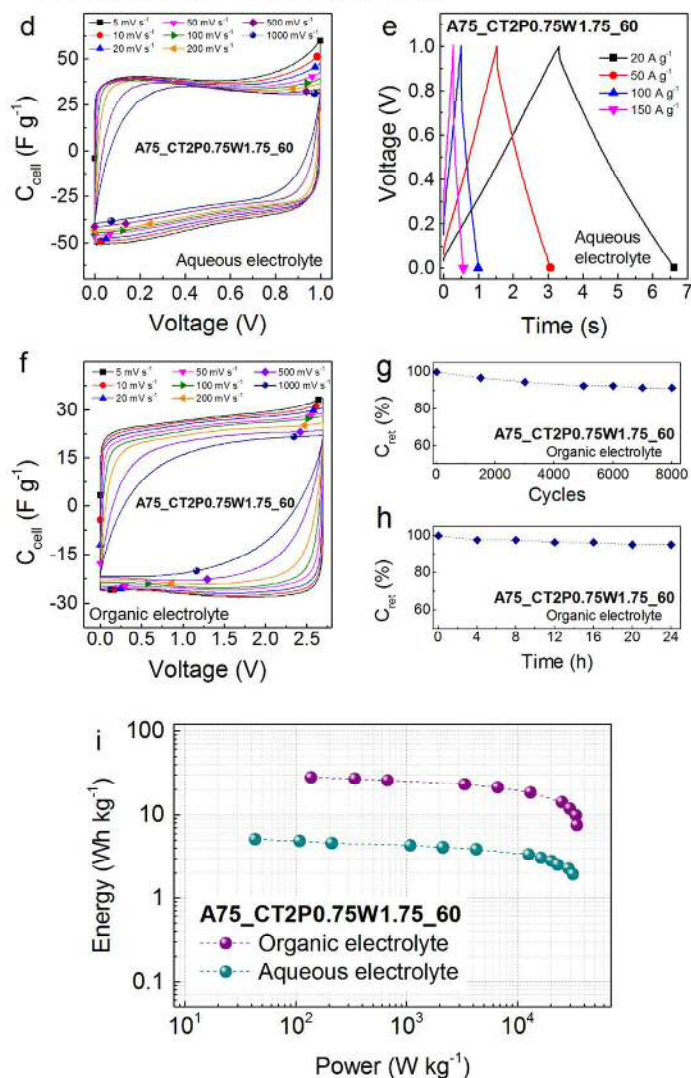


Figure 4(a) Set of water drops on CT2P1W2\_60, the insert shows a WCA = 157.4°, a video is provided as SI. (b) Adsorption of heptane by CT2P1W2\_60 in 40s, a video is provided as SI. (c) CO<sub>2</sub> adsorption capacities, at 0.1 MPa and 0 °C, as a function of micropore volume for materials from this study and for materials reported in the open literature.<sup>5-7</sup> Electrochemical characterization of A75\_CT2P0.75W1.75\_60 in 1 M H<sub>2</sub>SO<sub>4</sub> aqueous electrolyte: (d) evolution of CV curves with scan rate ranging from 5 to 1000 mV s<sup>-1</sup> and (e) GCD curves for current densities from 20 to 150 A g<sup>-1</sup>. Electrochemical tests of A75\_CT2P0.75W1.75\_60 in 1 M TEABF<sub>4</sub>/AN electrolyte: (f) CVs curves for scan rates from 5 to 1000 mV s<sup>-1</sup>; (g) capacity retention with number of cycles at 5 A g<sup>-1</sup>; and (h) capacity retention with time at 2.7 V. (i) Ragone plot of A75\_CT2P0.75W1.75\_60 using H<sub>2</sub>SO<sub>4</sub> and TEABF<sub>4</sub>/AN electrolytes.

of  $C_{cell}$ , 37 F g<sup>-1</sup> at 0.2 A g<sup>-1</sup> ( $C_e$ , of 148 F g<sup>-1</sup>). The smooth access to the micropores through the ordered mesoporous structure is proved by a great capacity retention,  $C_{ret}$ , of 64 %

when the current is increased up to 170 A g<sup>-1</sup> (see again Figure S11a).

Electrochemical characterization was also carried out in 1 M TEABF<sub>4</sub>/acetonitrile, an organic electrolyte commonly used in

commercial devices, within a potential window of 2.7 V. Figure 4f shows the CVs from 5 to 1000 mV s<sup>-1</sup> correspondent to  $C_{cell}$  from 27 to 17 F g<sup>-1</sup> ( $C_e$  from 108 to 57 F g<sup>-1</sup>), a capacity retention of 53 % was observed at 1 V s<sup>-1</sup>. The good rate capability is confirmed by the charge/discharge experiments, which show a capacitance retention of 49 % when the current density is increased from 0.2 to 70 A g<sup>-1</sup> (Figure S11b). The robustness of the supercapacitor based on the tannin-derived OMC is supported by a capacitance retention of 91 % after 8000 charge/discharge cycles at 5 A g<sup>-1</sup> (Figure 4g) and 95 % when holding the voltage at 2.7 V for 24 h (Figure 4h).<sup>58-61</sup>

Figure 4i shows the Ragone plot, usually employed for evaluating the performance of electrodes for batteries or capacitors. In aqueous electrolyte, the maximum energy density was 5 Wh kg<sup>-1</sup> with a power output of 43 W kg<sup>-1</sup> at a current density of 0.2 A g<sup>-1</sup>. In organic electrolyte, the performance of A75\_CT2P0.75W1.75\_60 considerably improved. The maximum energy density reached 28 Wh kg<sup>-1</sup> with a power output of 138 W kg<sup>-1</sup> at a current density of 0.2 A g<sup>-1</sup>. For a high power of 34 kW kg<sup>-1</sup>, the supercapacitor is able to deliver 7 Wh kg<sup>-1</sup>. The good electrochemical performance of the activated tannin-derived OMC is supported by the comparison to state-of-the-art micro/mesoporous or mesoporous carbons provided in Table S5.<sup>59,62-70</sup>

## Conclusion

A water-assisted mechanosynthesis method was described for preparing ordered mesoporous carbons (OMCs) from tannins. It is an easy and fast, one-pot method, only requiring 1 h of ball-milling without any additional drying or curing step before carbonization. Furthermore, the method is environment-friendly, due to the use of a natural and renewable carbon precursor and to the absence of toxic or hazardous substances during the synthesis. As a supplementary advantage, tailored OMCs with perfect 2D hexagonal geometry can be produced by modifying the surfactant to water weight ratio. The resultant OMCs, with an initial BET area of ~600 m<sup>2</sup> g<sup>-1</sup>, proved to be thermally stable under inert atmosphere up to 1500 °C, maintaining their 2D hexagonal geometry with minimum changes of peak mesopore width; while, upon activation the BET area increased up to ~1900 m<sup>2</sup> g<sup>-1</sup> and the peak position remained unaltered. These materials should find relevant applications in environmental remediation strategies for oil spills, in selective CO<sub>2</sub> adsorption from humid gases or as electrodes of supercapacitors using aqueous or organic electrolytes, among others.

## Experimental

**Materials.** Commercial mimosa tannin extract, kindly provided by the company SilvaChimica (St Michele Modovi, Italy) and available on the market under the name Fintan OP, was used as carbon precursor. Such tannin extract (T) is a light-brown powder that contains 80-82 % of phenolic (flavonoid) material. Pluronic® F127 (P) from Sigma-Aldrich was used as the pore-

directing agent. P is a triblock copolymer based on a hydrophobic polypropylene oxide (PPO) chain and two hydrophilic polyethylene oxide (PEO) chains that can form micelles in the presence of water (W). 1 M Aqueous solution of HCl from Sigma-Aldrich was used for the pH studies.

**Mechanosynthesis.** Several groups of samples were prepared by changing independently one of the following synthesis parameters: milling time, pH of added water, and P:W weight ratio. In all syntheses reported herein, the same amount of T (2 g) was systematically used as carbon precursor, added to the rest of components, and milled in a PM 100 planetary ball-milling machine (Retsch). The device was equipped with a 50 mL agate milling bowl and 10 agate balls of diameter 1 cm, and was used at a constant rotation speed of 500 rpm. For pH studies, aqueous solutions of HCl with different concentrations (0.1, 0.01, 0.001 and 0.0001 M) were prepared from a commercial solution (1 M).

**Heat treatment.** Paste-like materials retrieved from the mill were carbonized immediately after synthesis, without further drying or additional steps. The carbonization was performed under nitrogen flow (100 mL min<sup>-1</sup>) in a tubular furnace, using a quartz boat in a quartz tube (inner diameter 3.4 cm) heated up to 900 °C at a rate of 1 °C min<sup>-1</sup>. The final temperature was held for 1 h, and then the samples were left to cool down naturally under nitrogen flow. Pyrolysis at higher temperatures (1100, 1300 and 1500 °C) were carried out in another tubular furnace, using a ceramic boat in an alumina tube (inner diameter 7.5 cm) flushed with argon at the same flow rate as before. The temperature was again increased at 1 °C min<sup>-1</sup>, the set point was maintained for 1 h, and the samples were cooled down under argon at a rate of 3 °C min<sup>-1</sup>.

**Physical activation.** CO<sub>2</sub> activation was performed in the same quartz tube and the same tubular furnace as for carbonization at 900 °C. The temperature was first increased up to 900 °C under nitrogen flow (5 °C min<sup>-1</sup>, 100 mL min<sup>-1</sup>), then the gas was changed to CO<sub>2</sub> (50 mL min<sup>-1</sup>) and maintained for 75 min. Finally, the gas was changed again to nitrogen and the sample was left to cool down naturally until room temperature.

**Chemical activation.** KOH activation was carried out in a stainless steel tubular oven (inner diameter 15 cm) at 800 °C for 1 h under nitrogen flow (5 °C min<sup>-1</sup>, 150 mL min<sup>-1</sup>). Previously, the selected OMCs were impregnated with a KOH solution in order to obtain KOH to OMC weight ratios from 3 to 6. Activated OMCs were thoroughly washed with distilled water and 1 M HCl aqueous solution; a final drying at 105 °C was performed overnight. Chemical activation with CH<sub>3</sub>CO<sub>2</sub>K was performed by milling together the same quantities (2 g) of T, P, W and this salt, during 60 min. Carbonization was performed as for the OMCs, described above. CH<sub>3</sub>CO<sub>2</sub>K activated OMCs were washed as the KOH activated ones.

**Fourier-transform infrared (FTIR) and thermogravimetric analysis (TGA).** FTIR spectra were acquired using a Frontier Spotlight 400 (Perkin Elmer) spectrometer in transmission mode, using a range of wavenumbers from 650 to 4000 cm<sup>-1</sup>. TGA was performed under inert atmosphere (argon) with an STA 449F3 Jupiter (Netzsch) microbalance, with which samples (~15 mg) were heated at 10 °C min<sup>-1</sup> up to 900 °C.

**Pore texture analysis.** Nitrogen (N<sub>2</sub>) and carbon dioxide (CO<sub>2</sub>) adsorption isotherms at -196 °C and 0 °C, respectively, were obtained with ASAP 2020 and ASAP 2420 (Micromeritics) automatic adsorption devices, respectively. Samples were degassed under vacuum before adsorption analysis during at least 48 h at 110 °C. Using Microactive® and SAIEUS® software provided by Micromeritics, the following parameters were calculated: (i) BET area from the Brunauer–Emmet–Teller method,  $A_{BET}$  (m<sup>2</sup> g<sup>-1</sup>); (ii) total pore volume,  $V_{0.97,N_2}$  (cm<sup>3</sup> g<sup>-1</sup>); (iii) specific surface area and micropore volume by application of the non-local density functional theory (NLDFT) to N<sub>2</sub> and CO<sub>2</sub> isotherms,  $S_{NLDFT}$  (m<sup>2</sup> g<sup>-1</sup>) and  $V_{\mu,NLDFT}$  (cm<sup>3</sup> g<sup>-1</sup>), respectively; and (iv) mesopore volume,  $V_{meso}$  (cm<sup>3</sup> g<sup>-1</sup>) =  $V_{0.97,N_2} - V_{\mu,NLDFT}$ . Also, the pore-size distribution (PSD) in the mesopore range was calculated using the Barret–Joyner–Halenda (BJH) method with the Kruk–Jaroniec–Sayari (KJS) correction applied to the desorption branch of the N<sub>2</sub> isotherms. Mathematical analysis of the PSD was performed with the peak analyzer toolbox of OriginPro 9 software. Lorentzian peaks were used for the fitting, and maximum height (M), full width at half maximum (FWHM), and peak position (PP) were calculated for each peak.

**Transmission electron microscopy (TEM).** Investigations of the mesoporous structure of the carbons were carried out using a JEM - ARM 200F Cold FEG TEM/STEM operating at 200 kV and equipped with a spherical aberration (Cs) probe and image correctors. Before observation, the carbon powder was dispersed in ethanol using a low-power sonication bath for a few minutes, and a single drop of solution was deposited onto the carbon-coated copper TEM grid (200 mesh).

**Raman spectroscopy.** The nanotexture of the OMCs was studied from Raman spectra obtained with a Horiba Scientific XploRa Raman spectrometer, based on samples without preparation and investigated with a 50× objective. The Raman-scattered light was dispersed by a holographic grating with 1200 lines per mm and detected by a CCD camera. A laser of wavelength 532 nm, circularly polarized and filtered at 10% of its nominal power, was used. Such attenuation led to an incident power (~1.8 mW) that was too low to heat or damage the samples. Each spectrum was obtained by accumulation of 2 spectra recorded from 800 to 2200 cm<sup>-1</sup> over 180 s. Deconvolution of bands was carried out with the Labspec6 software from Horiba.

**Electrochemical characterization.** Electrochemical measurements were carried out using a VMP3 (Bio-Logic) electrochemical workstation. Disc-shaped electrodes with a diameter of 0.8 cm, thickness of ~ 130 μm and carbon loading of 5 – 5.5 mg cm<sup>-2</sup> were obtained from a paste prepared by mixing the OMC under study with polytetrafluoroethylene (PTFE) and carbon black in respective 85:10:5 weight ratios. The electrodes were then thoroughly impregnated with aqueous solution of H<sub>2</sub>SO<sub>4</sub> (1 M) or TEABF<sub>4</sub>/acetonitrile (1 M) as electrolytes. Symmetric two-electrode cells were used to study the capacitive behavior of the carbon materials, for which two working electrodes of comparable mass, separated by a porous glass fiber mat, were placed between two gold (H<sub>2</sub>SO<sub>4</sub>) or stainless steel (TEABF<sub>4</sub>/AN) current collectors. Cyclic

voltammetry (CV) and galvanostatic charge-discharge (GCD) tests were performed at a potential window between 0 and 1 V in the case of the aqueous electrolyte and 0 and 2.7 V in the case of the organic electrolyte. Scan rates ranging from 5 to 1000 mV s<sup>-1</sup> were applied for CV tests, and GCD experiments were carried out by varying the charge-discharge current density from 0.2 to 170 A g<sup>-1</sup>. The equations used to calculate the specific cell and electrode capacitances ( $C_{cell}$  and  $C_e$ , respectively) and the energy and power densities ( $E$  and  $P$ , respectively) are detailed on the Electronic Supplementary Information (ESI).

## Conflicts of interest

There are no conflicts to declare.

## Acknowledgements

Jimena Castro-Gutiérrez gratefully acknowledges CONACYT-SENER for the assigned scholarship to support her Ph.D. studies, resulting in the work presented herein.

## References

- 1 Y. Zhou, L. Tang, G. Zeng, J. Chen, Y. Cai, Y. Zhang, G. Yang, Y. Liu, C. Zhang and W. Tang, *Biosensors and Bioelectronics*, 2014, **61**, 519–525.
- 2 W. Libbrecht, A. Verberckmoes, J. W. Thybaut, P. Van Der Voort and J. De Clercq, *Carbon*, 2017, **116**, 528–546.
- 3 Y. Luo, S. Jiang, Q. Xiao, C. Chen and B. Li, *Scientific Reports*, , DOI:10.1038/s41598-017-07583-0.
- 4 Y. Xiang, Y. Pang, X. Jiang, J. Huang, F. Xi and J. Liu, *Applied Surface Science*, 2018, **428**, 338–347.
- 5 L. K. C. de Souza, N. P. Wickramaratne, A. S. Ello, M. J. F. Costa, C. E. F. da Costa and M. Jaroniec, *Carbon*, 2013, **65**, 334–340.
- 6 B. Zhu, K. Qiu, C. Shang and Z. Guo, *Journal of Materials Chemistry A*, 2015, **3**, 5212–5222.
- 7 J. Ludwinowicz and M. Jaroniec, *Carbon*, 2015, **94**, 673–679.
- 8 Y. Zhai, Y. Dou, D. Zhao, P. F. Fulvio, R. T. Mayes and S. Dai, *Advanced Materials*, 2011, **23**, 4828–4850.
- 9 Z. Yang, J. Ren, Z. Zhang, X. Chen, G. Guan, L. Qiu, Y. Zhang and H. Peng, *Chemical Reviews*, 2015, **115**, 5159–5223.
- 10 J. Lee, J. Kim and T. Hyeon, *Advanced Materials*, 2006, **18**, 2073–2094.
- 11 H. Chang, S. H. Joo and C. Pak, *Journal of Materials Chemistry*, 2007, **17**, 3078.
- 12 J. Lee, S. Han and T. Hyeon, *Journal of Materials Chemistry*, 2004, **14**, 478–486.
- 13 X. Cai, G. Zhu, W. Zhang, H. Zhao, C. Wang, S. Qiu and Y. Wei, *European Journal of Inorganic Chemistry*, 2006, **2006**, 3641–3645.
- 14 Y. Xia, W. Zhang, Z. Xiao, H. Huang, H. Zeng, X. Chen, F. Chen, Y. Gan and X. Tao, *Journal of Materials Chemistry*, 2012, **22**, 9209–9215.
- 15 H.-J. Liu, X.-M. Wang, W.-J. Cui, Y.-Q. Dou, D.-Y. Zhao and Y.-Y. Xia, *Journal of Materials Chemistry*, 2010, **20**, 4223.
- 16 Y. Meng, D. Gu, F. Zhang, Y. Shi, L. Cheng, D. Feng, Z. Wu, Z. Chen, Y. Wan, A. Stein and D. Zhao, *Chemistry of Materials*, 2006, **18**, 4447–4464.
- 17 Y. Huang, H. Cai, T. Yu, X. Sun, B. Tu and D. Zhao, *Chemistry – An Asian Journal*, 2007, **2**, 1282–1289.
- 18 X. Wang, C. Liang and S. Dai, *Langmuir*, 2008, **24**, 7500–7505.

- 19 S. Schlienger, A.-L. Graff, A. Celzard and J. Parmentier, *Green Chem.*, 2012, **14**, 313–316.
- 20 F. L. Braghiroli, V. Fierro, J. Parmentier, A. Pasc and A. Celzard, *Green Chem.*, 2016, **18**, 3265–3271.
- 21 S. L. James, C. J. Adams, C. Bolm, D. Braga, P. Collier, T. Friščić, F. Grepioni, K. D. M. Harris, G. Hyett, W. Jones, A. Krebs, J. Mack, L. Maini, A. G. Orpen, I. P. Parkin, W. C. Shearouse, J. W. Steed and D. C. Waddell, *Chem. Soc. Rev.*, 2012, **41**, 413–447.
- 22 G.-W. Wang, *Chemical Society Reviews*, 2013, **42**, 7668–7700.
- 23 G. Kaupp, *CrystEngComm*, 2009, **11**, 388–403.
- 24 K. Tanaka and F. Toda, *Chemical Reviews*, 2000, **100**, 1025–1074.
- 25 Q. Wang, Y. Mu, W. Zhang, L. Zhong, Y. Meng and Y. Sun, *RSC Advances*, 2014, **4**, 32113–32116.
- 26 G. Kaupp, *CrystEngComm*, 2011, **13**, 3108.
- 27 J. Zhu, J. Yang, R. Miao, Z. Yao, X. Zhuang and X. Feng, *J. Mater. Chem. A*, 2016, **4**, 2286–2292.
- 28 P. Zhang, L. Wang, S. Yang, J. A. Schott, X. Liu, S. M. Mahurin, C. Huang, Y. Zhang, P. F. Fulvio, M. F. Chisholm and S. Dai, *Nature Communications*, 2017, **8**, 15020.
- 29 A. Ricci, K. J. Olejar, G. P. Parpinello, P. A. Kilmartin and A. Versari, *Applied Spectroscopy Reviews*, 2015, **50**, 407–442.
- 30 G. Tondi and A. Petutschnigg, *Industrial Crops and Products*, 2015, **65**, 422–428.
- 31 J. Coates, *Encyclopedia of analytical chemistry*.
- 32 C. Liang, K. Hong, G. A. Guiochon, J. W. Mays and S. Dai, *Angewandte Chemie International Edition*, 2004, **43**, 5785–5789.
- 33 F. Xu, Y. Chen, M. Tang, H. Wang, J. Deng and Y. Wang, *ACS Sustainable Chemistry & Engineering*, 2016, **4**, 4473–4479.
- 34 F. L. Braghiroli, V. Fierro, J. Parmentier, L. Vidal, P. Gadonneix and A. Celzard, *Industrial Crops and Products*, 2015, **77**, 364–374.
- 35 K. Mortensen, *EPL (Europhysics Letters)*, 1992, **19**, 599.
- 36 K. Mortensen and J. S. Pedersen, *Macromolecules*, 1993, **26**, 805–812.
- 37 K. Mortensen and W. Brown, *Macromolecules*, 1993, **26**, 4128–4135.
- 38 G. Wanka, H. Hoffmann and W. Ulbricht, *Macromolecules*, 1994, **27**, 4145–4159.
- 39 M. Almgren, W. Brown and S. Hvidt, *Colloid & Polymer Science*, 1995, **273**, 2–15.
- 40 K. Mortensen and Y. Talmon, *Macromolecules*, 1995, **28**, 8829–8834.
- 41 P. Alexandridis and T. A. Hatton, *Colloids and Surfaces A: Physicochemical and Engineering Aspects*, 1995, **96**, 1–46.
- 42 K. Mortensen, *Journal of Physics: Condensed Matter*, 1996, **8**, A103–A124.
- 43 K. Mortensen, *Polymers for Advanced Technologies*, 2001, **12**, 2–22.
- 44 G. Riess, *Progress in Polymer Science*, 2003, **28**, 1107–1170.
- 45 S. Liu and L. Li, *ACS Applied Materials & Interfaces*, 2015, **7**, 2688–2697.
- 46 S. Liu and L. Li, *Colloids and Surfaces A: Physicochemical and Engineering Aspects*, 2015, **484**, 485–497.
- 47 D. Long, W. Qiao, L. Zhan, X. Liang and L. Ling, *Microporous and Mesoporous Materials*, 2009, **121**, 58–66.
- 48 J. Jin, N. Nishiyama, Y. Egashira and K. Ueyama, *Microporous and Mesoporous Materials*, 2009, **118**, 218–223.
- 49 J. Xu, A. Wang and T. Zhang, *Carbon*, 2012, **50**, 1807–1816.
- 50 Z. Yang, X. Gu and X. Liang, *Computer Modeling in Engineering & Sciences*, 2011, **74**, 161–181.
- 51 B. Smarsly, A. Gibaud, W. Ruland, D. Sturmayr and C. J. Brinker, *Langmuir*, 2005, **21**, 3858–3866.
- 52 M. I. Nathan, J. E. Smith and K. N. Tu, *Journal of Applied Physics*, 1974, **45**, 2370–2370.
- 53 R. O. Dillon, J. A. Woollam and V. Katkanant, *Physical Review B*, 1984, **29**, 3482.
- 54 A. C. Ferrari and J. Robertson, *Physical review B*, 2000, **61**, 14095.
- 55 A. Szczurek, A. Ortona, L. Ferrari, E. Rezaei, G. Medjahdi, V. Fierro, D. Bychanok, P. Kuzhir and A. Celzard, *Carbon*, 2015, **88**, 70–85.
- 56 M. M. Khin, A. S. Nair, V. J. Babu, R. Murugan and S. Ramakrishna, *Energy & Environmental Science*, 2012, **5**, 8075.
- 57 D. N. H. Tran, S. Kabiri, T. R. Sim and D. Losic, *Environmental Science: Water Research & Technology*, 2015, **1**, 298–305.
- 58 R. Shao, J. Niu, J. Liang, M. Liu, Z. Zhang, M. Dou, Y. Huang and F. Wang, *ACS Applied Materials & Interfaces*, 2017, **9**, 42797–42805.
- 59 A. B. Fuertes and M. Sevilla, *ACS Applied Materials & Interfaces*, 2015, **7**, 4344–4353.
- 60 J. Xia, N. Zhang, S. Chong, D. Li, Y. Chen and C. Sun, *Green Chemistry*, 2018, **20**, 694–700.
- 61 Y. Cao, L. Xie, G. Sun, F. Su, Q.-Q. Kong, F. Li, W. Ma, J. Shi, D. Jiang, C. Lu and C.-M. Chen, *Sustainable Energy & Fuels*, 2018, **2**, 455–465.
- 62 A. Sanchez-Sanchez, M. T. Izquierdo, J. Ghanbaja, G. Medjahdi, S. Mathieu, A. Celzard and V. Fierro, *Journal of Power Sources*, 2017, **344**, 15–24.
- 63 A. Sanchez-Sanchez, A. Martinez de Yuso, F. L. Braghiroli, M. T. Izquierdo, E. D. Alvarez, E. Pérez-Cappe, Y. Mosqueda, V. Fierro and A. Celzard, *RSC Advances*, 2016, **6**, 88826–88836.
- 64 M. Rose, Y. Korenblit, E. Kockrick, L. Borchardt, M. Oschatz, S. Kaskel and G. Yushin, *Small*, 2011, **7**, 1108–1117.
- 65 K. Wang, Y. Song, R. Yan, N. Zhao, X. Tian, X. Li, Q. Guo and Z. Liu, *Applied Surface Science*, 2017, **394**, 569–577.
- 66 W. Xing, S. Z. Qiao, R. G. Ding, F. Li, G. Q. Lu, Z. F. Yan and H. M. Cheng, *Carbon*, 2006, **44**, 216–224.
- 67 D. Kang, Q. Liu, J. Gu, Y. Su, W. Zhang and D. Zhang, *ACS Nano*, 2015, **9**, 11225–11233.
- 68 M. Sevilla, S. Álvarez, T. A. Centeno, A. B. Fuertes and F. Stoeckli, *Electrochimica Acta*, 2007, **52**, 3207–3215.
- 69 X. He, P. Ling, J. Qiu, M. Yu, X. Zhang, C. Yu and M. Zheng, *Journal of Power Sources*, 2013, **240**, 109–113.
- 70 H.-J. Liu, W.-J. Cui, L.-H. Jin, C.-X. Wang and Y.-Y. Xia, *Journal of Materials Chemistry*, 2009, **19**, 3661.

## Synthesis of Perfectly Ordered Mesoporous Carbons by Water-assisted Mechanochemical Self-assembly of Tannin

Castro-Gutiérrez et al.

### TABLE OF CONTENTS



Water-assisted mechanochemical synthesis allows preparing perfectly ordered mesoporous carbons from tannins without crosslinkers or any drying or curing step

## Supplementary Information

## Synthesis of Perfectly Ordered Mesoporous Carbons by Liquid-assisted Mechanochemical Self-assembly of Tannin

Jimena Castro-Gutiérrez,<sup>a</sup> Angela Sanchez-Sanchez,<sup>a</sup> Jaafar Ghanbaja,<sup>a</sup> Noel Díez,<sup>b</sup> Marta Sevilla,<sup>b</sup> Alain Celzard<sup>a</sup> and Vanessa Fierro<sup>a\*</sup>

<sup>a</sup> Institute Jean Lamour, UMR CNRS, University of Lorraine, ENSTIB, 27 Rue Philippe Séguin, BP 21042, 88051 Epinal Cedex 9, France.

<sup>b</sup> Instituto Nacional del Carbón (CSIC), P.O. Box 73, Oviedo, 33080, Spain.

**Table S1.** Pore texture parameters, calculated from N<sub>2</sub> and CO<sub>2</sub> adsorption isotherms, of carbon materials: (i) prepared with various amounts of Pluronic® F127 and water, and used as references; (ii) obtained after various milling times; and (iii) synthesized with 2 g of aqueous HCl solutions with different pH values.

	Milling time [min]	[ ]	[ ]	[ ]	[ ]	[ ]	[%]
(i) References							
CT2P0W0_60	60	829	578	0.25	0.23	0.02	8
CT2P0W2_60	60	503	231	0.10	0.11	—	—
CT2P2W0_60	60	672	466	0.36	0.17	0.19	53
(ii) Milling time							
CT2P2W2_30	30	735	543	0.46	0.18	0.28	60
CT2P2W2_45	45	683	497	0.46	0.16	0.30	64
CT2P2W2_60	60	695	522	0.47	0.16	0.30	65
CT2P2W2_75	75	703	521	0.44	0.17	0.27	61
CT2P2W2_90	90	709	538	0.46	0.18	0.28	61
CT2P2W2_120	120	663	484	0.40	0.16	0.24	60
(iii) pH							
CT2P2pH0_60	60	775	591	0.43	0.20	0.23	53
CT2P2pH1_60	60	713	533	0.51	0.17	0.34	67
CT2P2pH2_60	60	696	522	0.45	0.17	0.28	61
CT2P2pH3_60	60	713	528	0.44	0.18	0.26	60
CT2P2pH4_60	60	698	524	0.45	0.17	0.28	62

and : specific surface areas calculated by applying NLDFT and BET models, respectively; : total single point pore volume at relative pressure of 0.97; : micropore volume from NLDFT model; : mesopore volume; : mesopore fraction.

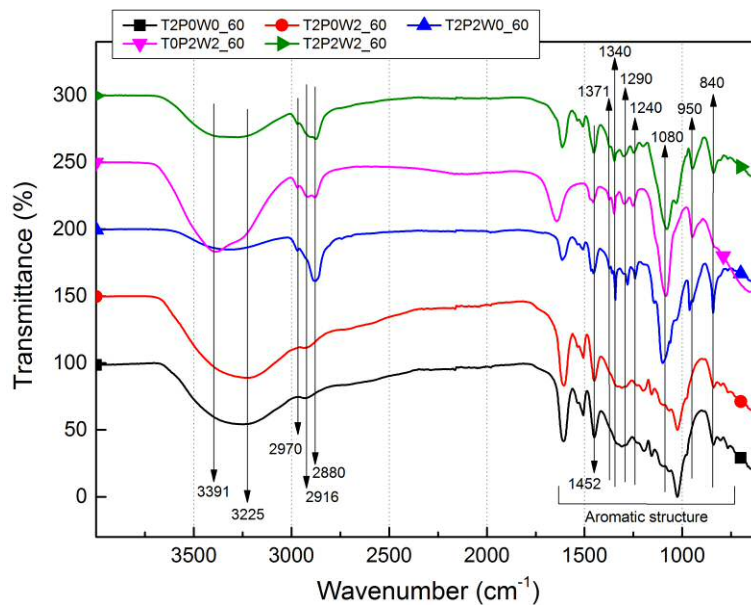


**Figure S1.** FTIR spectra of T2P2W2\_60 and reference samples. The data were normalized with respect to a common peak ( $1452\text{ cm}^{-1}$ ) and, for easier viewing, the spectra were shifted with respect to each other by 50% of transmittance.

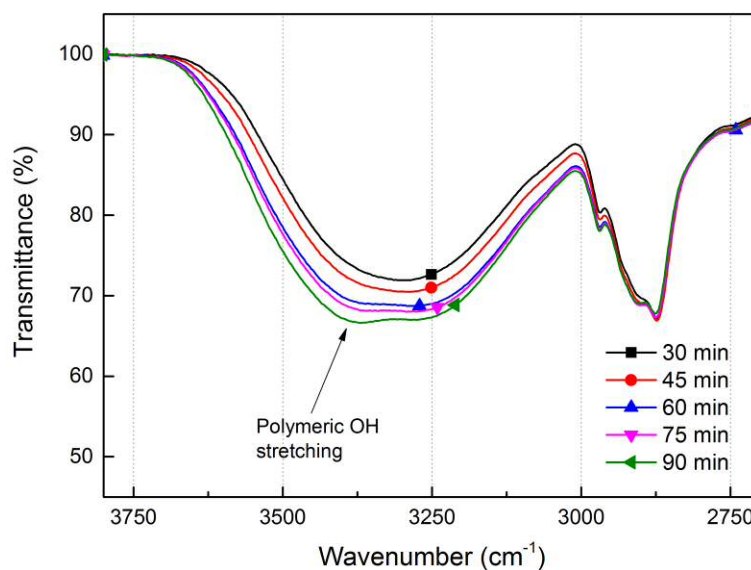


**Figure S2.** Detailed view of the FTIR spectra of samples T2P2W2\_t synthesized during different milling times t, ranging from 30 to 90 min. For comparison, the data were normalized with respect to a common peak ( $1452\text{ cm}^{-1}$ ).

**Table S2.** Peak assignment of FTIR spectra presented in Figure S1 and Figure S2.<sup>1-3</sup>

Aromatic structure of mimosa tannin	
Wavenumber [cm <sup>-1</sup> ]	Assignment
1606 <sup>a)</sup> , 1533, 1507	C=C stretching in pyrogallol-like B ring
1450 <sup>b)</sup>	C-C stretching in pyrogallol-like B ring
1200	C-O stretching of aromatic rings
1157 <sup>c)</sup>	Vibrations of resorcinol-like A ring
1025 <sup>c)</sup>	Overlapping stretching of C-O, C-C, C-OH, C-H bonds
766	Torsion of resorcinol-like A ring

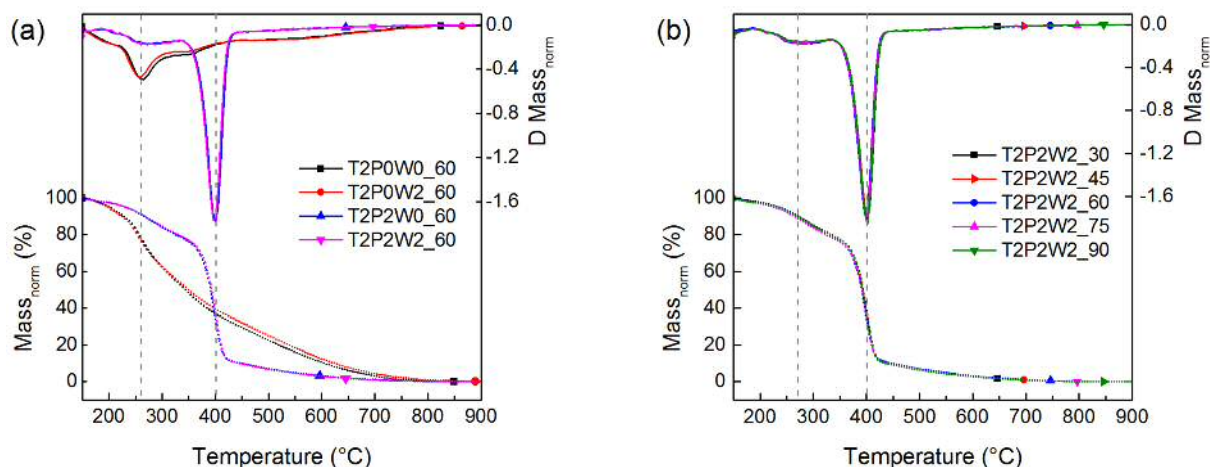
  

Triblock copolymer Pluronic® F127	
Wavenumber [cm <sup>-1</sup> ]	Assignment
3391	Polymeric OH stretching
2970, 2916, 2880, 1371, 1340, 950, 840	C-H bonds
1290, 1240, 1080	C-O bonds

<sup>a)</sup> Some authors assigned this peak to OH bending or C=O stretching,<sup>1</sup> explaining why a peak around 1640 cm<sup>-1</sup> also appears in T0P2W2\_60 spectrum.

<sup>b)</sup> This peak appears also in T0P2W2\_60 spectrum because of the C-C bonds; however, the intensity is lower in comparison with the samples containing tannin.

<sup>c)</sup> Low-intensity peak. For samples containing P, this peak overlaps the strong peak at 1080 cm<sup>-1</sup> due to the C-O bonds.



**Figure S3.** Absolute (left scale) and differential (right scale) normalized mass losses of: (a) T2P2W2\_60 and reference samples; and (b) samples T2P2W2<sub>t</sub> prepared at various milling times *t*, ranging from 30 to 90 min. The normalization was performed after removing the mass loss attributed to the evaporation of water.

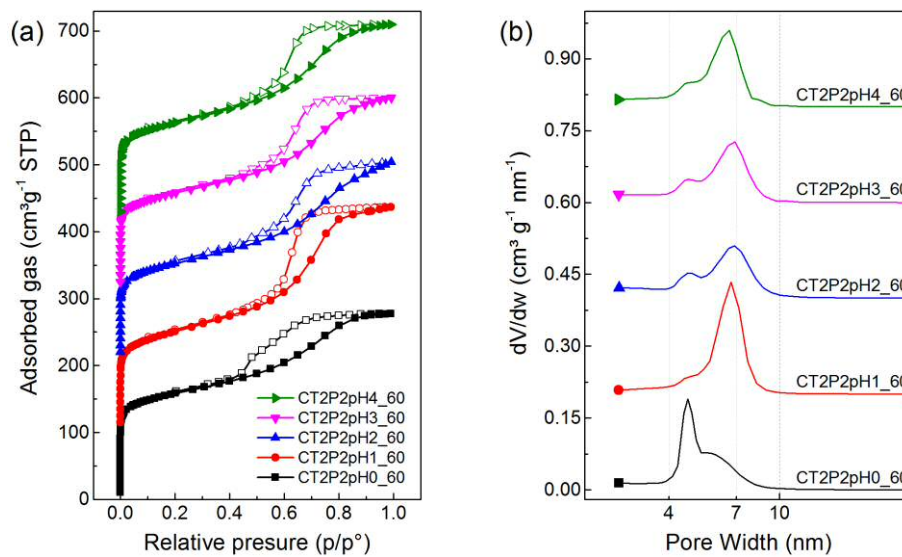


**Figure S4.** (a) N<sub>2</sub> adsorption-desorption isotherms and (b) corresponding PSDs of carbon materials CT2P2pH<sub>x</sub>\_60, synthesized by using aqueous solutions of HCl at pH ranging from 0 to 4 instead of water, and a milling time of 60 min. For easier viewing, the curves were shifted with respect to each other by 105 cm<sup>3</sup> g<sup>-1</sup> STP for isotherms and by 0.2 cm<sup>3</sup> g<sup>-1</sup> nm<sup>-1</sup> for PSDs.

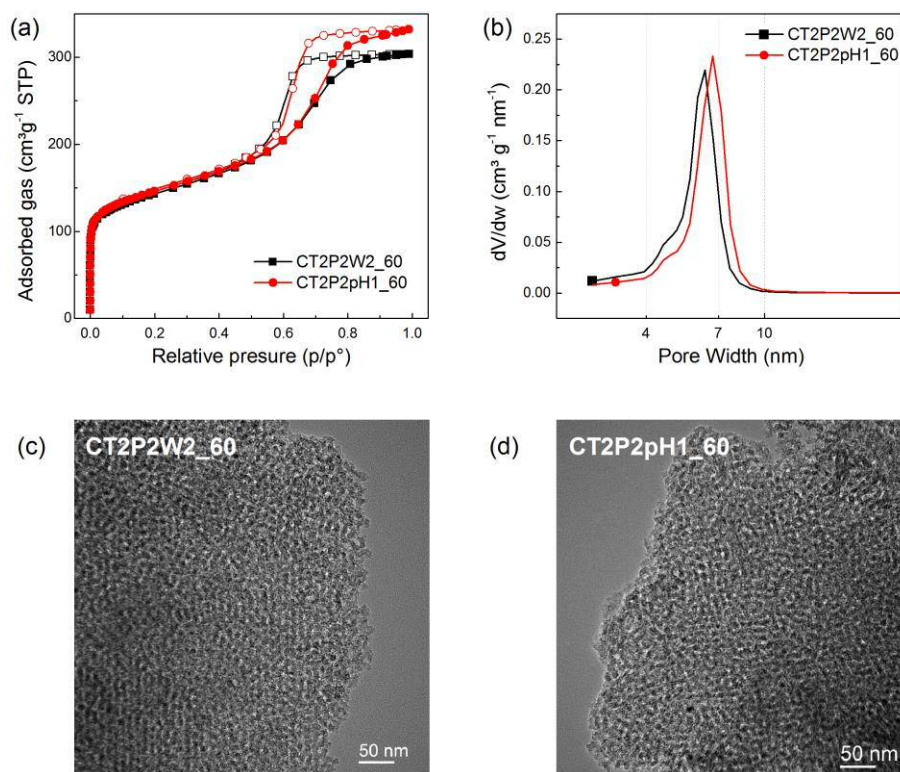


**Figure S5.** Comparison between CT2P2W2\_60 and CT2P2pH1\_60: (a) N<sub>2</sub> adsorption-desorption isotherms; (b) PSDs; and (c,d) TEM images.

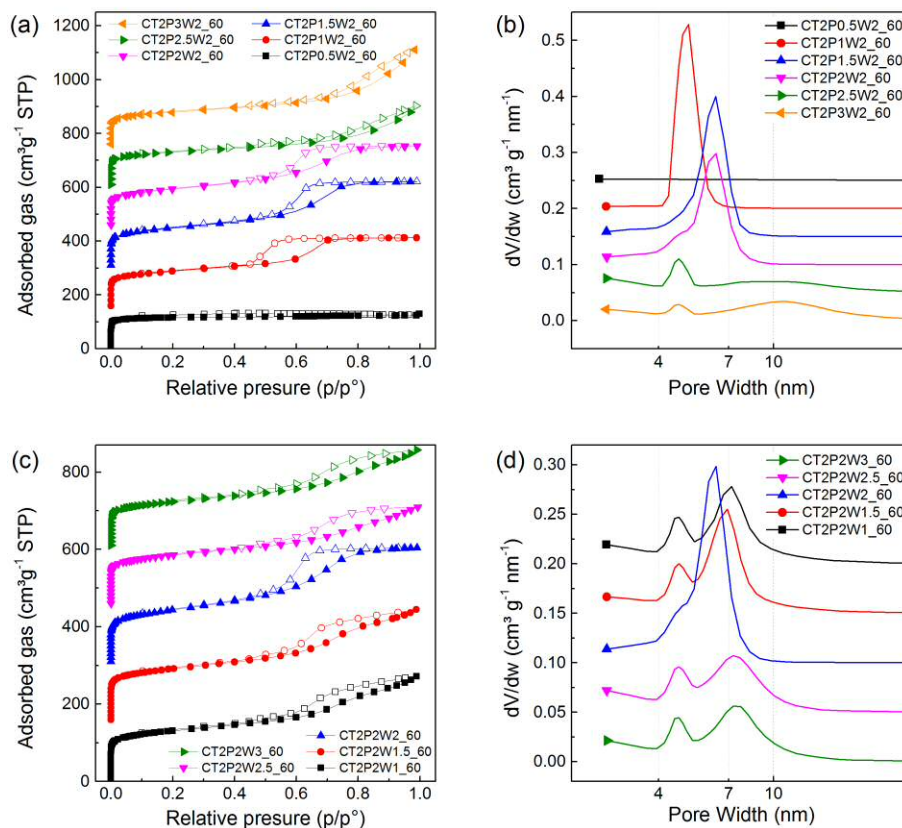


Figure S6. (a,c)  $\text{N}_2$  adsorption-desorption isotherms and (b,d) corresponding PSDs of carbon materials synthesized using 60 min of milling and various P:W weight ratios. For easier viewing, the curves were shifted with respect to each other by  $150 \text{ cm}^3 \text{ g}^{-1} \text{ STP}$  for isotherms and by  $0.05 \text{ cm}^3 \text{ g}^{-1} \text{ nm}^{-1}$  for PSDs.

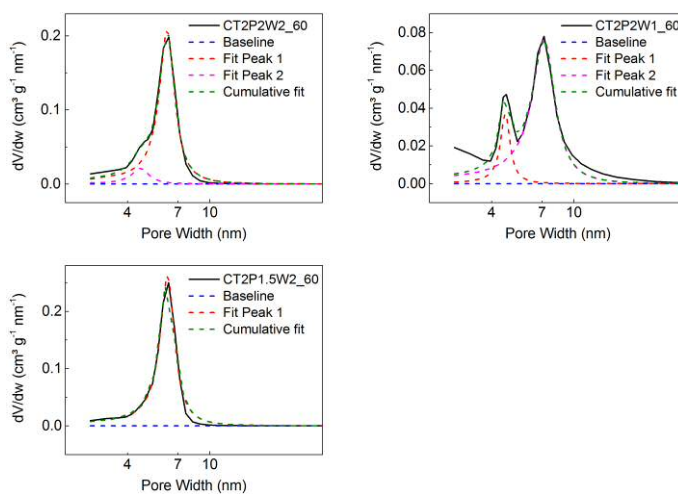


Figure S7. Examples of deconvolution into Lorentzian contributions performed on the PSDs of CT2P2W2\_60, CT2P2W1\_60 and CT2P1.5W2\_60 samples.

Table S3. Characteristics of the main peaks in the PSDs of carbon materials synthesized using 60 min of milling and various P:W weight ratios.

	Maximum height (M) [cm <sup>3</sup> g <sup>-1</sup> nm <sup>-1</sup> ]	FWHM [nm]	M / FWHM	Peak position [nm]
CT2P0W2_60	0.0	--	0.0	--
CT20.5W2_60	0.0	--	0.0	--
CT2P1W2_60	0.37	0.73	0.50	5.0
CT2P1.5W2_60	0.26	1.24	0.21	6.2
CT2P2W2_60	0.02 0.23	1.13 1.20	0.02 0.19	4.7 6.2
CT2P2.5W2_60	0.05 0.02	0.51 17.22	0.10 0.001	4.7 10.3
CT2P3W2_60	0.02 0.03	0.48 10.65	0.03 0.003	4.7 11.3
CT2P2W0_60	0.03 0.03	0.44 7.40	0.06 0.004	4.7 7.0
CT2P2W1_60	0.04 0.08	0.61 2.21	0.06 0.03	4.7 7.1
CT2P2W1.5_60	0.04 0.11	0.59 1.84	0.06 0.06	4.7 6.8
CT2P2W2.5_60	0.03 0.06	0.63 3.42	0.05 0.02	4.7 7.4
CT2P2W3_60	0.03 0.06	0.58 3.37	0.06 0.02	4.6 7.6
CT2P0.5W1_60	0.0	--	0.0	--
CT2P0.5W1.5_60	0.09	0.71	0.12	4.1
CT2P0.75W1.25_60	0.25	0.54	0.46	4.4
CT2P0.75W1.5_60	0.44	0.37	1.20	4.5
CT2P0.75W1.75_60	0.56	0.32	1.77	4.6
CT2P1W1_60	0.31	0.87	0.35	4.7
CT2P1W1.25_60	0.34	0.82	0.42	5.0
CT2P1W1.5_60	0.47	0.60	0.78	4.9
CT2P1W1.75_60	0.31	0.94	0.33	5.2
CT2P1.25W1.25_60	0.29	0.99	0.29	5.9
CT2P1.25W1.5_60	0.25	1.21	0.21	6.0
CT2P1.25W1.75_60	0.23	1.26	0.18	5.9
CT2P1.5W1_60	0.27	1.21	0.22	6.2
CT2P1.5W1.25_60	0.25	1.35	0.18	6.1
CT2P1.5W1.5_60	0.31	1.04	0.30	6.2
CT2P1.5W1.75_60	0.30	1.11	0.27	6.1

Table S4. Pore texture parameters of samples synthesized with different P:W initial ratios and obtained after 60 min of ball-milling, calculated from N<sub>2</sub> and CO<sub>2</sub> isotherms.

	( )	( )	( )	( )	( )	(%)
<b>CT2P0.5W1_60</b>	566	304	0.12	0.13	--	--
<b>CT2P0.5W1.5_60</b>	732	529	0.25	0.20	0.05	18
<b>CT2P0.5W2_60</b>	657	457	0.19	0.18	0.01	3
<b>CT2P0.75W1.25_60</b>	659	477	0.30	0.17	0.12	41
<b>CT2P0.75W1.5_60</b>	731	537	0.35	0.19	0.15	44
<b>CT2P0.75W1.75_60</b>	761	567	0.36	0.20	0.16	44
<b>CT2P1W1_60</b>	733	546	0.42	0.18	0.24	57
<b>CT2P1W1.25_60</b>	755	568	0.44	0.19	0.25	57
<b>CT2P1W1.5_60</b>	750	556	0.44	0.19	0.25	58
<b>CT2P1W1.75_60</b>	784	587	0.47	0.19	0.28	59
<b>CT2P1W2_60</b>	712	508	0.41	0.17	0.24	58
<b>CT2P1.25W1.25_60</b>	713	532	0.46	0.17	0.29	63
<b>CT2P1.25W1.5_60</b>	732	547	0.49	0.17	0.31	64
<b>CT2P1.25W1.75_60</b>	696	527	0.45	0.17	0.28	62
<b>CT2P1.5W1_60</b>	742	565	0.51	0.18	0.34	66
<b>CT2P1.5W1.25_60</b>	715	539	0.49	0.17	0.32	66
<b>CT2P1.5W1.5_60</b>	767	588	0.52	0.18	0.34	65
<b>CT2P1.5W1.75_60</b>	750	577	0.53	0.18	0.35	66
<b>CT2P1.5W2_60</b>	726	541	0.50	0.17	0.33	66
<b>CT2P2W1_60</b>	689	486	0.40	0.17	0.23	58
<b>CT2P2W1.5_60</b>	721	524	0.44	0.18	0.26	60
<b>CT2P2W2_60</b>	695	522	0.47	0.16	0.30	65
<b>CT2P2W2.5_60</b>	696	503	0.39	0.18	0.21	54
<b>CT2P2W3_60</b>	641	454	0.38	0.16	0.22	59
<b>CT2P2.5W2_60</b>	686	486	0.43	0.17	0.26	60
<b>CT2P3W2_60</b>	638	476	0.53	0.16	0.37	70

and : specific surface areas calculated by applying NLDFT and BET models, respectively; : total single point pore volume at relative pressure of 0.97; : micropore volume from NLDFT model; : mesopore volume; : mesopore fraction.

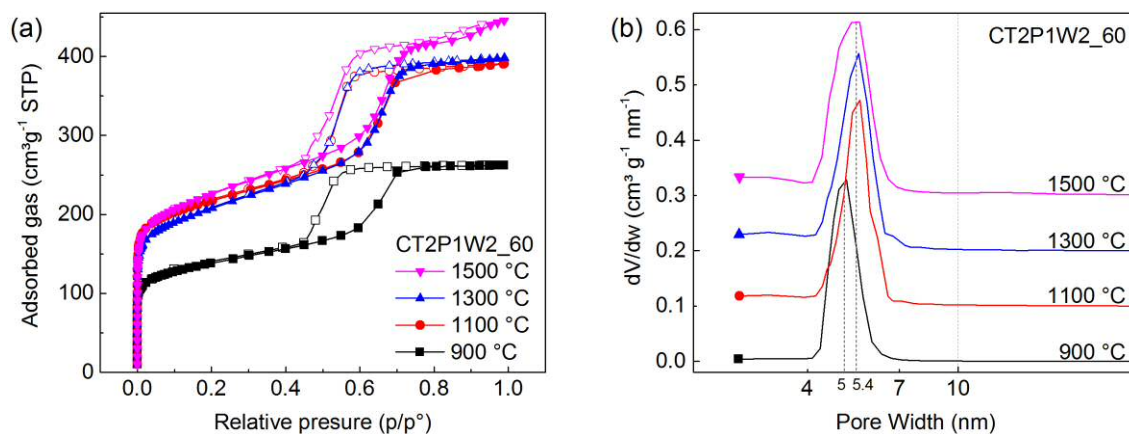


Figure S8. (a)  $N_2$  adsorption-desorption isotherms and (b) corresponding PSDs for CT2P1W2\_60 pyrolyzed at different temperatures. For easier viewing, the PSDs curves were shifted with respect to each other by  $0.1 cm^3 g^{-1} nm^{-1}$ .

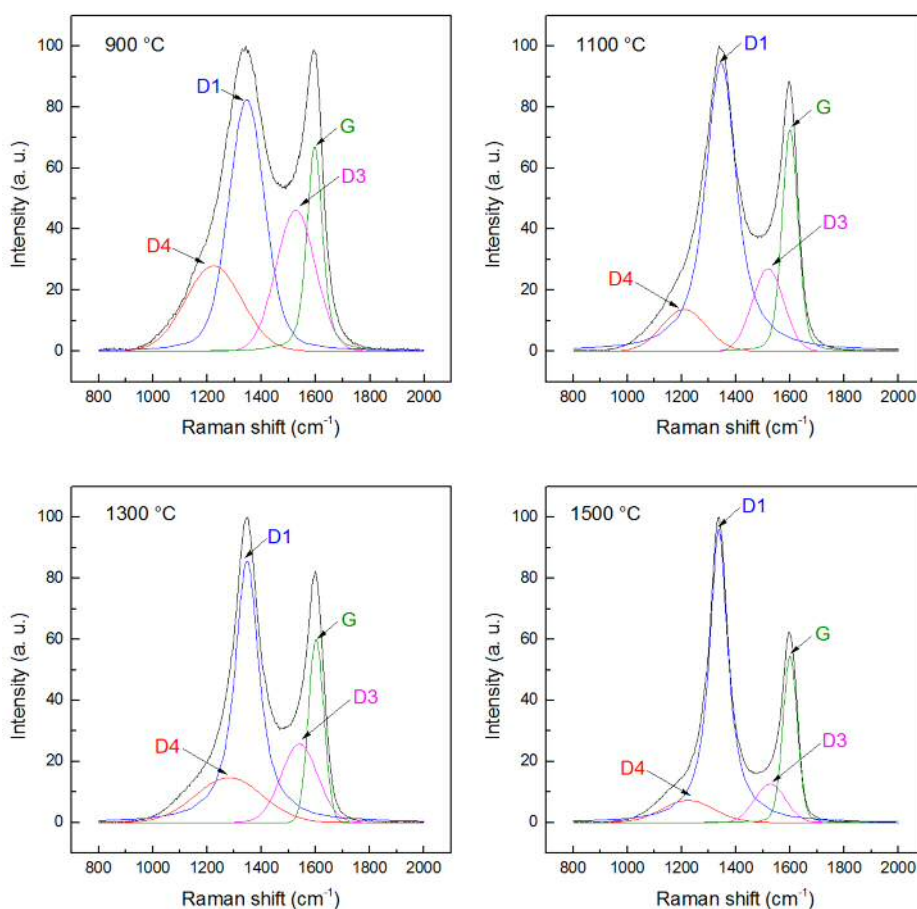


Figure S9. Raman spectra of CT2P1W2\_60 pyrolyzed at different temperatures, and corresponding D<sub>1</sub>, D<sub>3</sub>, D<sub>4</sub> and G bands.

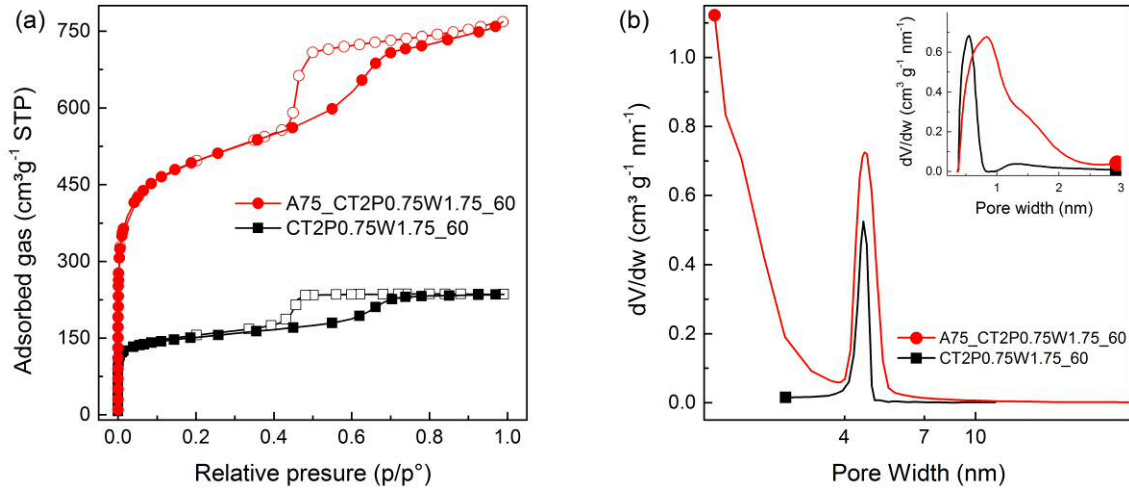


Figure S10. (a)  $N_2$  adsorption-desorption isotherms, and (b) corresponding PSD for one OMC before (CT2P0.75W1.75\_60) and after (A75\_CT2P0.75W1.75\_60) activation with  $CO_2$  for 75 min at  $900^\circ C$ . The inset in (b) shows the DFT PSD in the micropore range for both materials.

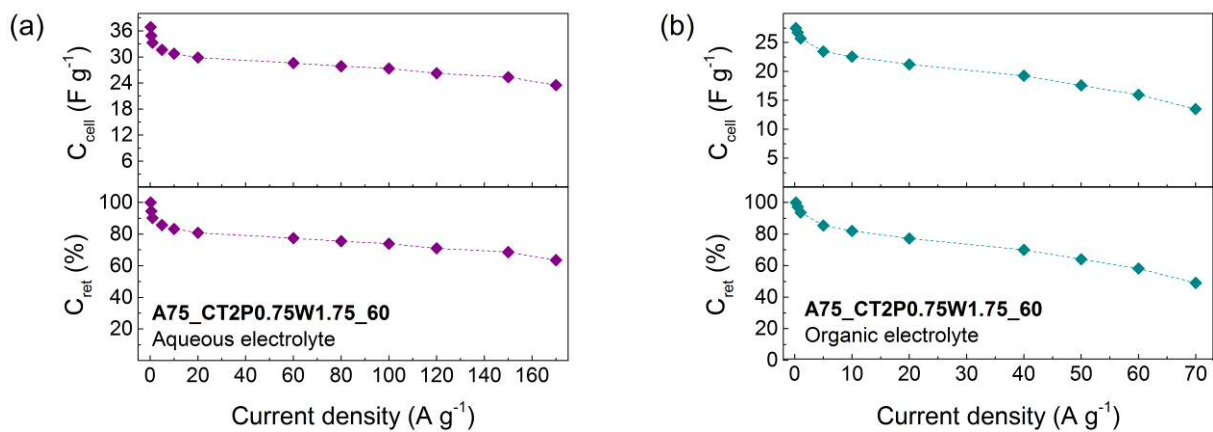


Figure S11. Evolution of cell capacitance ( $C_{cell}$ ) and capacitance retention ( $C_{ret}$ ) with current density for A75\_CT2P0.75W1.75\_60 in (a) aqueous and (b) organic electrolyte.

Table S5. Electrochemical performances of different carbon materials reported in the literature.

Carbon precursor/ Synthesis method	Carbon material	Electrolyte (cell voltage)	Capacitance [F g <sup>-1</sup> ]	Current density [A g <sup>-1</sup> ]	Energy density [Wh kg <sup>-1</sup> ]	Power density [kW kg <sup>-1</sup> ]	Ref. in ESI (Ref. in article)
Polyphenols: Phloroglucinol, gallic acid, catechin, and mimosa tannin/ Hard-templating (SBA-15); carbonization	OMCs: 2D- Hexagonal.	1 M H <sub>2</sub> SO <sub>4</sub> (0.8 V)	~196	0.1	2.27 – 4.08	6.83 – 0.06	4
			~127	12	2.46 – 4.46	5.97 – 0.05	(62)
					1.31 – 4.18	5.17 – 0.01	
					1.91 – 4.62	6.56 – 0.06	
Sugarcane molasses/ HTC; carbonization	Oxygen rich carbons.	1 M H <sub>2</sub> SO <sub>4</sub> (0.7 V)	32	0.1	~0.04 – ~1.8	3 – ~0.15	5
			13	1	~0.35 – ~6.9	~5.5 – 0.5	(63)
					~0.03 – ~0.6	~4.5 – ~0.15	
					~0.45 – ~6.9	~5 – ~0.13	
Mesoporous SiC/ Si etching	Microporous nanorods	1 M H <sub>2</sub> SO <sub>4</sub> (0.6 V)	~150 – ~190	0.1	-	-	6
			~130 – 150	15.5			(64)
Willow catkins/ Carbonization; KOH activation	Hollow fibrous structure.	6 M KOH (1 V)	333 <sup>a</sup> 209 <sup>a</sup>	0.1 10	5 – 8.8	5 – 0.05	7 (65)
Sucrose/ Hard-templating (MCM-48 and SBA-15); carbonization	OMCs: 3D cubic, 2D hexagonal rods and 2D hexagonal pipes.	30 wt.% KOH (0.9 V)	-	-	~4 – ~6	~0.8 – ~0.1	8
					~4.7 – ~5.4	~0.95 – ~0.1	(66)
					~5.4 – ~5.9	~1.05 – ~0.1	
Seaweed/ Carbonization; KOH activation	Micro- mesoporous carbon with egg-box structure	1 M H <sub>2</sub> SO <sub>4</sub> (1 V)	425	0.1	-	-	9
			280	100			(67)
			210 156	0.1 50	25 – 42	29 – 0.39	
		1M TEABF <sub>4</sub> /AN (2.5 V)					

Table S5 (Continued). Electrochemical performances of different carbon materials reported in the literature.

Carbon precursor/ Synthesis method	Carbon material	Electrolyte (cell voltage)	Capacitance [F g <sup>-1</sup> ]	Current density [A g <sup>-1</sup> ]	Energy density [Wh kg <sup>-1</sup> ]	Power density [kW kg <sup>-1</sup> ]	Ref. in ESI (Ref. in article)
Sodium gluconate/ Carbonization	Micro- mesoporous carbon nanosheets	1 M H <sub>2</sub> SO <sub>4</sub> (1 V)	175 – 220 80 – 140	0.05 150	~1 – ~6 ~1.5 – ~6 ~3 – ~8	~20 – ~0.02 ~20 – ~0.02 ~30 – 0.02	10 (59)
		1M TEABF <sub>4</sub> /AN (2.7 V)	100 – 135 50 – 100	0.05 120	~7 – 23 ~13 – ~33 16 – ~26	~90 – ~0.07 110 – ~0.07 110 – ~0.07	
Furfuryl alcohol/ Hard templating (Silica)	OMCs: 3D cubic; 3D low ordered. Worwhole- like pores.	1M TEABF <sub>4</sub> /AN (2 V)	~95	~0.06	~3.5 – ~13	~5.7 – ~0.04	11 (68)
Peanut shell and rice husk/ ZnCl <sub>2</sub> activation	Disordered mesoporous carbons	1M TEABF <sub>4</sub> /PC (2.7 V)	99 79	0.05 3	19.3 – 26.6	1.01 – ~0.07	12 (69)
Resol and Pluronic/ Two-step template synthesis: latex spheres and silica hard template Thermosetting; carbonization; HF washing.	Ordered mesoporous carbon sphere arrays	1M TEABF <sub>4</sub> /PC (3 V)	84	0.1	-	-	13 (70)

<sup>a</sup> Capacitance values calculated from galvanostatic charge-discharge in a three-electrode cell.

### Calculation of electrochemical properties

The specific cell capacitances ( , F g<sup>-1</sup>) were calculated from CV data through Equation S1:

$$\text{---} \quad (1)$$

where is the current (A), is the scan rate (V s<sup>-1</sup>), is the potential window (V), and is the mass of active material in the two electrodes (g).

GCD curves were used to calculate the specific capacitances of the cell ( , F g<sup>-1</sup>), the energy densities ( , Wh kg<sup>-1</sup>) and the power densities ( , W kg<sup>-1</sup>) by application of Equation S2, S3 and S4, respectively:

$$\text{---} \quad (2)$$

$$\text{---} \quad (3)$$

$$\text{---} \quad (4)$$

where is the discharge current (A); is the discharge time (s), and is the potential drop due to inner resistance.

The single electrode specific capacitances, , can be estimated by Equation S5:

$$\text{---} \quad (5)$$

## References

- 1 A. Ricci, K. J. Olejar, G. P. Parpinello, P. A. Kilmartin and A. Versari, *Applied Spectroscopy Reviews*, 2015, **50**, 407–442.
- 2 G. Tondi and A. Petutschnigg, *Industrial Crops and Products*, 2015, **65**, 422–428.
- 3 J. Coates, *Encyclopedia of analytical chemistry*.
- 4 A. Sanchez-Sanchez, M. T. Izquierdo, J. Ghanbaja, G. Medjahdi, S. Mathieu, A. Celzard and V. Fierro, *Journal of Power Sources*, 2017, **344**, 15–24.
- 5 A. Sanchez-Sanchez, A. Martinez de Yuso, F. L. Braghiroli, M. T. Izquierdo, E. D. Alvarez, E. Pérez-Cappe, Y. Mosqueda, V. Fierro and A. Celzard, *RSC Advances*, 2016, **6**, 88826–88836.
- 6 M. Rose, Y. Korenblit, E. Kockrick, L. Borchardt, M. Oschatz, S. Kaskel and G. Yushin, *Small*, 2011, **7**, 1108–1117.
- 7 K. Wang, Y. Song, R. Yan, N. Zhao, X. Tian, X. Li, Q. Guo and Z. Liu, *Applied Surface Science*, 2017, **394**, 569–577.
- 8 W. Xing, S. Z. Qiao, R. G. Ding, F. Li, G. Q. Lu, Z. F. Yan and H. M. Cheng, *Carbon*, 2006, **44**, 216–224.
- 9 D. Kang, Q. Liu, J. Gu, Y. Su, W. Zhang and D. Zhang, *ACS Nano*, 2015, **9**, 11225–11233.
- 10 A. B. Fuertes and M. Sevilla, *ACS Applied Materials & Interfaces*, 2015, **7**, 4344–4353.
- 11 M. Sevilla, S. Álvarez, T. A. Centeno, A. B. Fuertes and F. Stoeckli, *Electrochimica Acta*, 2007, **52**, 3207–3215.
- 12 X. He, P. Ling, J. Qiu, M. Yu, X. Zhang, C. Yu and M. Zheng, *Journal of Power Sources*, 2013, **240**, 109–113.
- 13 H.-J. Liu, W.-J. Cui, L.-H. Jin, C.-X. Wang and Y.-Y. Xia, *Journal of Materials Chemistry*, 2009, **19**, 3661.